2007 Annual SCEC report

InSAR survey of Southern California: Secular and transient line-of-sight strain from stacks of ERS and ENVISAT data

Publications and abstracts resulted from this project:

Rivet, D. and Y. Fialko, Active deformation in the Eastern California Shear Zone: Implications from 15 years of InSAR observations, manuscript in preparation.

Fialko, Y., R. Lanari, M. Manzo, and F. Casu, Modern slip rates of the southern San Andreas and San Jacinto faults from time-series analysis of InSAR and GPS data, manuscript in preparation.

Barbot, S., Y. Hamiel, and Y. Fialko, Space geodetic investigation of the co- and post-seismic deformation due to the 2003 M_w 7.2 Altai earthquake: Implications for the local lithospheric rheology, J. Geophys. Res., 113, B03403, doi:10.1029/2007JB005063, 2008.

Rivet, D. and Y. Fialko, Interseismic secular deformation in Southern California from InSAR-derived maps over the time period between 1992 and 2006, Eos, Trans. AGU, 88(52), Suppl., abst. G51C-0620, 2007.

Fialko, Y., InSAR Measurements of Postseismic Deformation due to the Mojave Desert Earthquakes: Implications for the Driving Mechanisms, Eos, Trans. AGU, 88(52), Suppl., abst. G53A-02 (invited), 2007.

Hearn, E., Y. Fialko, and Y. Finzi, Mojave Compliant Zone Structure and Properties: Constraints from InSAR and Mechanical Models, Eos, Trans. AGU, 88(52), Suppl., abst. S34C-04 (invited), 2007.

Summary of results:

We analyzed a large InSAR dataset from Southern California focusing on a region adjacent to the Coachella Valley segment of the San Andreas fault (SAF) (*Fialko*, 2006). Precise quantification of deformation in this area is important due to a high seismic risk posed by the Southern San Andreas and San Jacinto faults. Also, a number of previous studies (using independent data and techniques) make this region a good target for comparing and contrasting results from various geodetic methods.

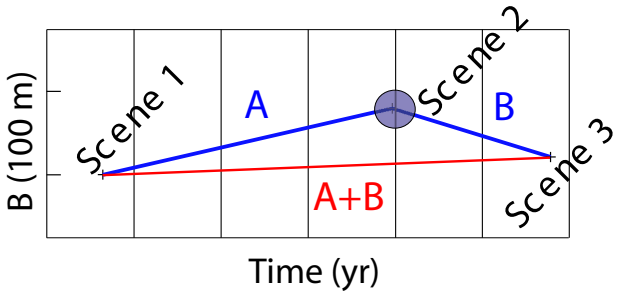

Figure 1: An example of three interferable SAR acquisitions. The Atmospheric Noise Coefficient for a shared acquisition (2) is defined by equation (2). Interferograms A and B represent a phase difference between acquisitions (2-1), and (3-2), respectively.

Because the main limitation of the InSAR measurements of small-amplitude ground velocities (centimeters per year or less) is the atmospheric noise (*Goldstein*, 1995; *Tarayre and Massonnet*, 1996; *Zebker et al.*, 1997), we developed a new method for stacking of multiple interferograms, which can effectively push InSAR technique toward it's theoretical accuracy limit of the line of sight (LOS) velocities of the order of a millimeter per year (e.g., *Fialko and Simons*, 2001; *Peltzer et al.*, 2001). Our method makes use of the fact that the phase contribution due to atmosphere changes sign in "consecutive" interferograms that share a common acquisition. By quantifying the magnitude of the sign-flipping phase we can identify SAR acquisitions that are highly affected by the atmospheric noise, and construct an optimal "stacking tree" that minimizes the contribution of such noisy scenes. The scheme entails the following steps:

1. Generate a set of interferograms for a given range of perpendicular baselines and time spans.

2. Select a subset of interferograms with sufficient correlation and coverage.

3. Evaluate Atmospheric Noise Coefficient (ANC) for each SAR acquisition. We do so by subdividing the interferometric "connectivity tree" into triplets, and computing some norm of range changes for every interferogram, as well as for sums of sequential interferograms sharing a common scene. Based on a number of experiments, we find that the root mean square (RMS) of the de-trended range changes ($\Delta\rho$), defined as

$$RMS = \sqrt{\frac{1}{N}\sum_{i=0}^{N}(\Delta\rho_i - T_i)^2}, \tag{1}$$

where N is the number of valid pixels and T is some best-fitting trend (e.g., a quadratic surface, or some other predictor of zero mean), performs well as the signal norm. Figure 1 and

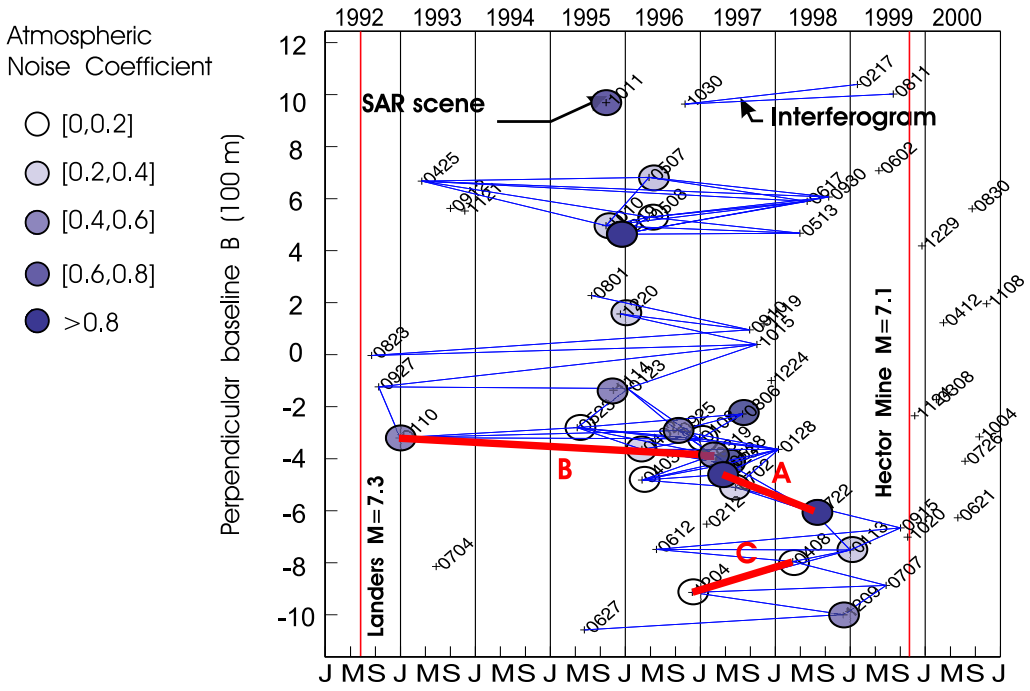

Figure 2: Interferometric pairs for the period between Landers and Hector Mine earthquakes from the ERS track 127. Horizontal axis represents time, and vertical axis represents perpendicular baseline (distance between repeated orbits). Lines connecting dots denote radar interferograms analyzed. Blue dots represent the Atmospheric Noise Coefficient evaluated using equation (2).

equation (2) illustrate how the Atmospheric Noise Coefficient is defined for each acquisition. For instance, for a data triplet (1,2,3), the Atmospheric Noise Coefficient of a scene 2 is given by

$$ANC_2 = \frac{1}{2}(RMS_A + RMS_B) - RMS_{A+B}. \tag{2}$$

We identify this coefficient for all shared SAR scenes in a data set. For scenes that are not shared (e.g., at the beginning and end of the catalog) ANC is estimated using a regression between (ANC_m-ANC_n) and RMS_{mn} (calculated for a given data set). Figure 2 shows an example of atmospheric noise estimation for the ERS track 127 (Mojave desert, eastern California), and Figure 3 illustrates several interferometric pairs for various inferred values of ANC.

4. Finally, we minimize the contribution of SAR acquisitions that were deemed noisy by re-arranging the "connectivity tree" around such acquisitions so that the number of "in-coming" and "out-going" connections is the same (Figure 4). Thus the contribution of noisy scenes is canceled out: interferograms involving noisy scenes are used in the stack, but such scenes

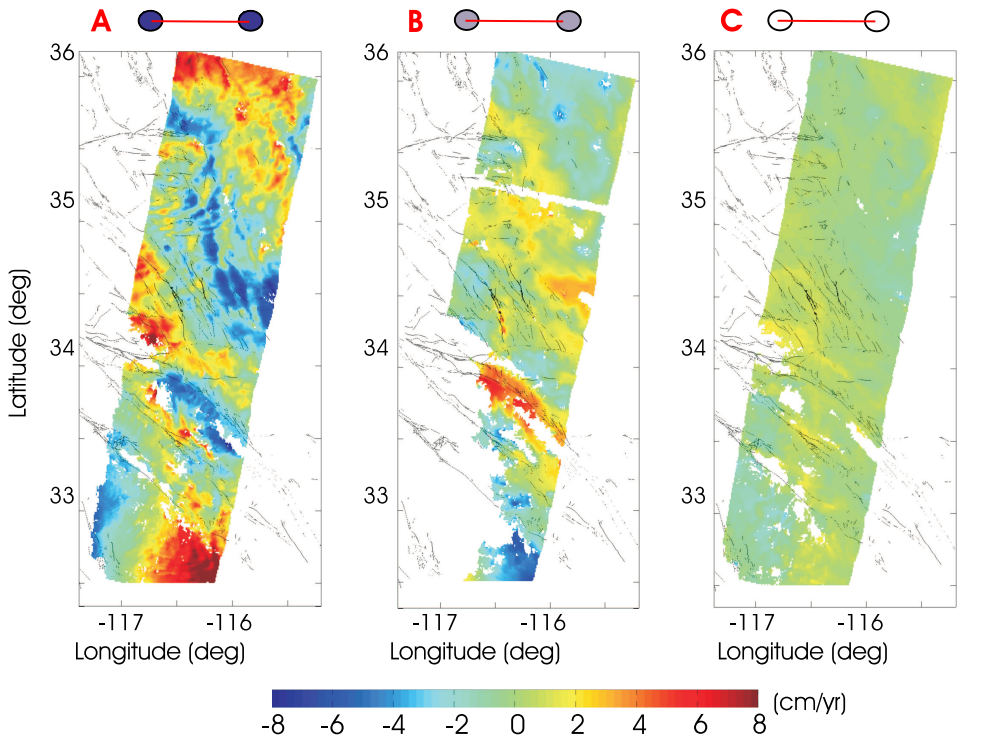

Figure 3: Examples of interferograms with various values of the Atmospheric Noise Coefficient (see red lines and notation in Figure 2).

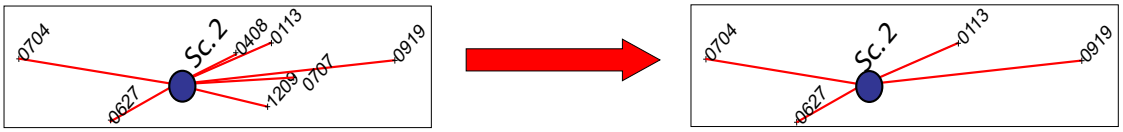

Figure 4: Partial elimination of interferograms to diminish a contribution of a "noisy" SAR scene.

do not affect the stacked radar phase. The degree of suppression (the difference between the in-coming and out-going connections) of a particular scene may be adjusted depending on the magnitude of ANC. Note that interferometric pairs affected by significant non-steady deformation - e.g., due to an earthquake - may be used for stacking upon subtracting the coseismic signal (using either a model or a shorter-term coseismic interferogram).

We have performed a comprehensive evaluation of the described algorithm by comparing results with those obtained using other techniques, as well as independent data, such as continuous GPS. In particular, we compared the mean velocity field computed using the ANR method to that obtained using the Small Baseline Subset (SBAS) method (*Berardino et al.*, 2002; *Casu et al.*, 2006). To perform this cross-validation, we collaborated with

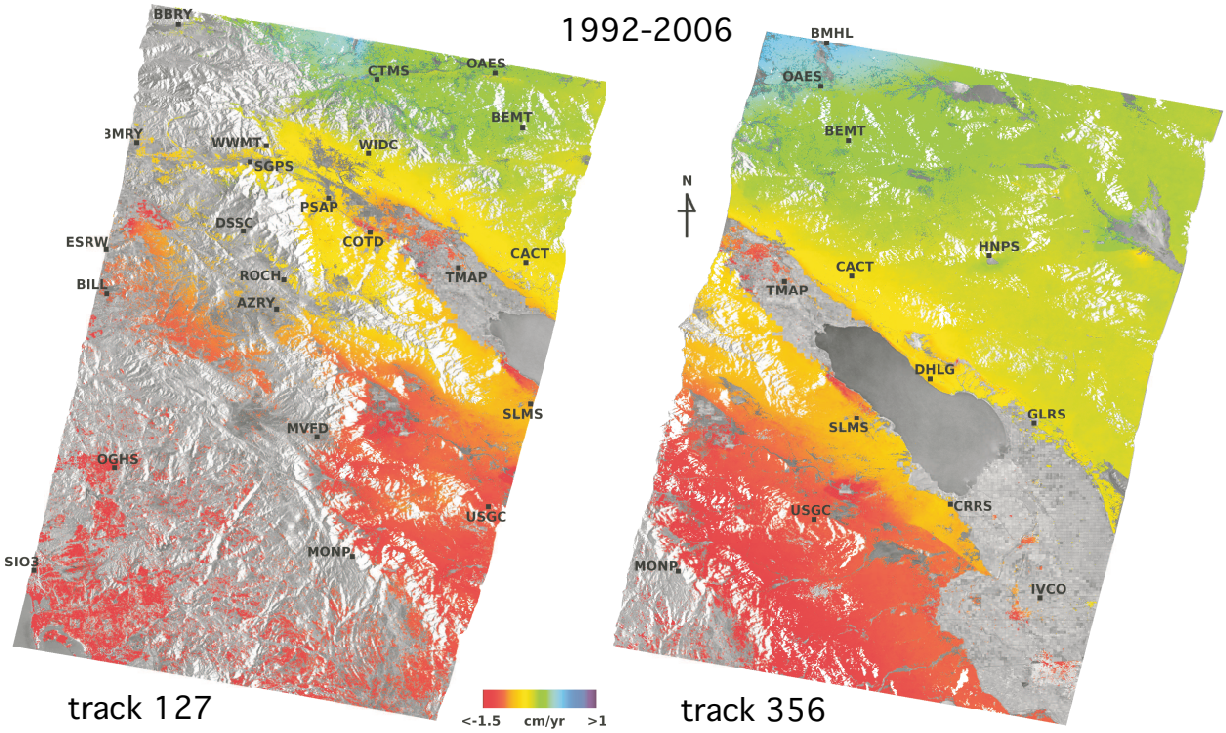

Figure 5: Average LOS velocity maps from the ERS tracks 127 (left) and 356 (right). Also shown are positions of continuous GPS sites used to cross-validate InSAR-derived velocity fields.

the InSAR research group at IREA, Italy. SBAS method computes time series of LOS displacements for every coherent pixel in a given set of interferograms. These time series can be then interpolated on a pixel by pixel basis to obtain a mean velocity map. Figure 5 shows mean LOS velocities from the ERS tracks 127 and 356 that span a 200-km stretch of the southern San Andreas Fault. InSAR data in both images represent average velocities of the Earth's surface over a time period of 15 years, between 1992 and 2006. Figure 6 shows LOS velocities across the southern San Andreas Fault (track 356, see *Fialko* (2006)) inferred using the two techniques. Velocities obtained using the two approaches are very similar; however, the ANR method is much more efficient computationally. The gain becomes even more dramatic for longer strips of data. These results lend support to our previous estimates of the present-day slip rate on the southern SAF of 25 ± 2 mm/yr *Fialko* (2006). Another robust test of the deformation pattern revealed by InSAR data from the ERS track 356 is provided by our analysis of independent data set from a neighboring track 127. Because

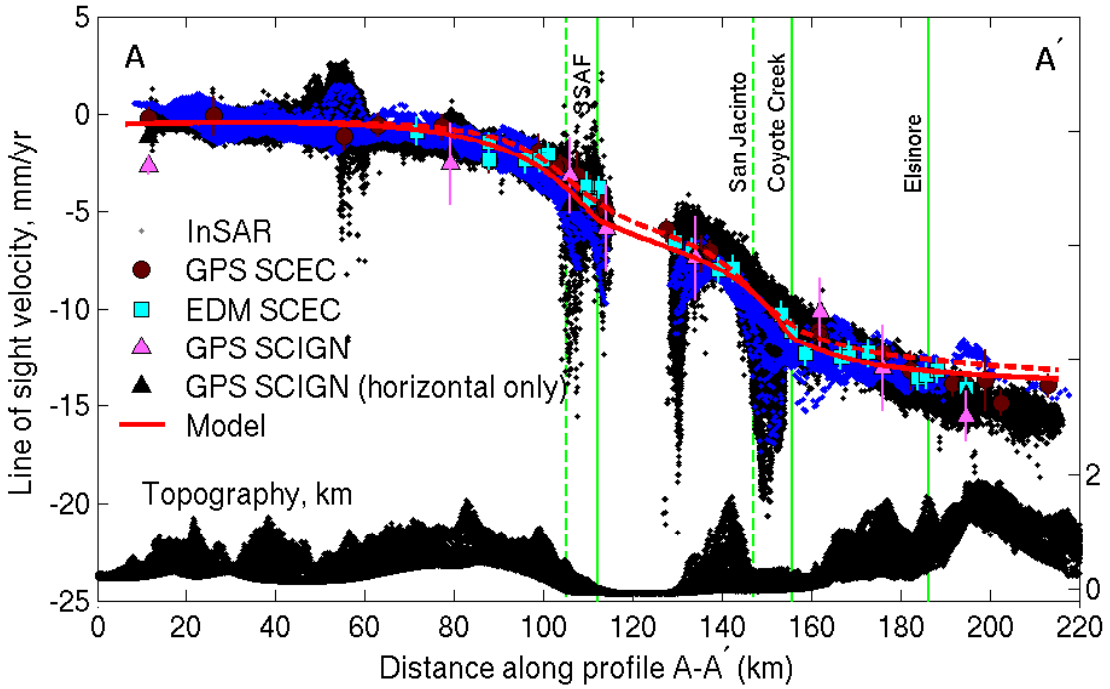

Figure 6: LOS velocities from a profile across the southern SAF (*Fialko*, 2006) over a time interval 1992-2006, as inferred from the SBAS time series analysis (black dots) and ANR method (blue dots).

of the overlap of adjacent satellite swathes, some area around the Salton Sea is imaged from both tracks. Data takes from different tracks are acquired on different dates, so that atmospheric contributions are completely uncorrelated. An overall similarity of the average LOS velocity field seen in Figure 5 confirms that these data indeed capture the dominant tectonic signal. In fact, subtle differences in the LOS velocity pattern (slightly lower LOS velocities inferred from track 127) are consistent with variations in the radar incidence angle across the radar image: somewhat smaller incidence angles in the near range (east side) of an image imply a smaller LOS component of the horizontal (strike-slip) motion of the ground, compared to the LOS component in the far range. Although data from track 127 are more affected by radar decorrelation (primarily, due to heavier vegetation), we are able to quantify the interseismic strain accumulation along the San Bernardino section of the SAF, as well as the northern San Jacinto fault (Figure 5). The data show a clear pattern of elastic strain accumulation on both faults (including the Anza Gap on the San Jacinto fault). This strain pattern can be readily interpreted in terms of present-day slip rates using numerical models

of interseismic deformation.

References

Berardino, P., G. Fornaro, R. Lanari, and E. Sansosti, A new algorithm for surface deformation monitoring based on small baseline differential SAR interferograms, *IEEE Trans. Geosci. Rem. Sens.*, *40*, 2375–2383, 2002.

Casu, F., M. Manzo, and R. Lanari, A quantitative assessment of the SBAS algorithm performance for surface deformation retrieval from DInSAR data, *Rem. Sens. Env.*, *102*, 195–210, 2006.

Fialko, Y., Interseismic strain accumulation and the earthquake potential on the southern San Andreas fault system, *Nature*, *441*, 968–971, 2006.

Fialko, Y., and M. Simons, Evidence for on-going inflation of the Socorro magma body, New Mexico, from Interferometric Synthetic Aperture Radar imaging, *Geophys. Res. Lett.*, *28*, 3549–3552, 2001.

Goldstein, R. M., Atmospheric limitations to repeat-track radar interferometry, *Geophys. Res. Lett.*, *22*, 2517–2520, 1995.

Peltzer, G., F. Crampe, S. Hensley, and P. Rosen, Transient strain accumulation and fault interaction in the Eastern California shear zone, *Geology*, *29*, 975–978, 2001.

Tarayre, H., and D. Massonnet, Atmospheric propagation heterogeneities revealed by ERS-1 interferometry, *Geophys. Res. Lett.*, *23*, 989–992, 1996.

Zebker, H. A., P. A. Rosen, and S. Hensley, Atmospheric effects in interferometric synthetic aperture radar surface deformation and topographic maps, *J. Geophys. Res.*, *102*, 7547–7563, 1997.